HHS Public Access

Author manuscript

Neuroimage. Author manuscript; available in PMC 2021 January 28.

Published in final edited form as:

Neuroimage. 2020 November 01; 221: 117188. doi:10.1016/j.neuroimage.2020.117188.

Optical imaging reveals functional domains in primate sensorimotor cortex

Robert M. Friedman[f], **Nicholas G. Chehade**[a,c,d], **Anna Wang Roe**[f,g], **Omar A. Gharbawie**[a,b,c,d,e,*]

[a]Systems Neuroscience Center, University of Pittsburgh, Pittsburgh, PA 15261, United States

[b]Department of Neurobiology, University of Pittsburgh, Pittsburgh, PA 15261, United States

[c]Center for Neuroscience, University of Pittsburgh, Pittsburgh, PA 15261, United States

[d]Center for Neural Basis of Cognition, University of Pittsburgh, Pittsburgh, PA 15261, United States

[e]Department of Bioengineering, University of Pittsburgh, Pittsburgh, PA 15261, United States

[f]Division of Neuroscience, Oregon National Primate Research Center, Oregon Health and Science University, Beaverton, OR 97006, United States

[g]Interdisciplinary Institute of Neuroscience and Technology, School of Medicine, Zhejiang University, Hangzhou, China

Abstract

Motor cortex (M1) and somatosensory cortex (S1) are central to arm and hand control. Efforts to understand encoding in M1 and S1 have focused on temporal relationships between neural activity and movement features. However, it remains unclear how the neural activity is spatially organized within M1 and S1. Optical imaging methods are well-suited for revealing the spatio-temporal organization of cortical activity, but their application is sparse in monkey sensorimotor cortex. Here, we investigate the effectiveness of intrinsic signal optical imaging (ISOI) for measuring cortical activity that supports arm and hand control in a macaque monkey. ISOI revealed spatial domains that were active in M1 and S1 in response to instructed reaching and grasping. The lateral M1 domains overlapped the hand representation and contained a population of neurons with peak firing during grasping. In contrast, the medial M1 domain overlapped the arm representation and a population of neurons with peak firing during reaching. The S1 domain overlapped the hand representations of areas 1 and 2 and a population of neurons with peak firing upon hand contact with the target. Our single unit recordings indicate that ISOI domains report the locations of spatial clusters of functionally related neurons. ISOI is therefore an effective tool for surveilling the neocortex for “hot zones” of activity that supports movement. Combining the strengths of ISOI with other imaging modalities (e.g., fMRI, 2-photon) and with electrophysiological methods can open new frontiers in understanding the spatio-temporal organization of cortical signals involved in movement control.

*Corresponding author at: Systems Neuroscience Center, University of Pittsburgh, Pittsburgh, PA 15261, United States., omar@pitt.edu (O.A. Gharbawie).

Keywords

Motor cortex; Somatosensory cortex; Reach; Grasp; Intrinsic signal optical imaging; Single unit recording

1. Introduction

The non-human primate arm and hand act together as a unit to accomplish essential tasks (e.g. feeding, grooming, climbing). The forelimb representations in primary motor cortex (M1) and in somatosensory cortex (S1) are central to the cortical network involved in controlling the arm and hand. Intracortical microstimulation (ICMS) studies in macaque monkeys have shown that the M1 forelimb representation has a somatotopic organization. Map details vary across reports, but in general the arm (shoulder and elbow) and hand (wrist and digits) are represented in contiguous zones with overlapping borders (Kwan et al., 1978; Sessle and Wiesendanger, 1982; Park et al., 2001). Similarly, each somatosensory area (areas 3a, 3b, 1, and 2) contains an orderly map of the forelimb that is accessible with receptive field mapping and multi-unit recordings (Nelson et al., 1980; Pons et al., 1985; Seelke et al., 2012). Given that coordinated arm/hand actions (e.g. reach-to-grasp) are predicated on the animation of joints in the arm and hand according to specific temporal structures, it stands to reason that neural activity that support arm/hand actions would follow specific spatio-temporal patterns within the forelimb representations.

Single unit recordings in M1 have informed much of our understanding about temporal relationships between neural activity and muscle activity, joint kinematics, and touch (Fetz and Cheney, 1980; Georgopoulos et al., 1986; Moran and Schwartz, 1999; Gardner et al., 2006; Hatsopoulos et al., 2007; Griffin et al., 2015). However, with few exceptions (e.g. Saleh et al., 2012; Riehle et al., 2013; Rouse and Schieber, 2016), the relationship between neural encoding and the spatial organization of M1 has been mostly overlooked. Consequently, the spatio-temporal organization of activity that occurs in M1 in the service of arm and hand actions is unknown. A similar knowledge gap is present for S1.

Imaging methods provide continuous sampling of cortical space and are therefore well-suited for this problem. However, cortical control of movement in primates has been scarcely investigated with any imaging modality (Nelissen and Vanduffel, 2011; Kondo et al., 2018). Our objective here was to determine whether ISOI could be used to surveille cortical activity that supports arm and hand movements in macaques. ISOI offers a number of strengths that we wished to exploit. (1) ISOI affords high spatial resolution (i.e., higher than fMRI) in a mesoscale field-of-view (i.e., wider than two-photon) that can cover most of the forelimb representations in M1 and S1. (2) ISOI has a well-established track record in investigations of cortical organization, particularly in early visual areas of anesthetized macaques (e.g., Grinvald et al., 1991; Lu et al., 2010). ISOI has also been used in awake/behaving macaques, albeit in paradigms that involve passive viewing (Grinvald et al., 1991) or saccadic responses (Tanigawa et al., 2010), which are less susceptible to motion artifact as compared to forelimb tasks. (3) ISOI results are spatially registered to blood vessel patterns, which facilitate precise electrode placement for parallel electrophysiological interrogation.

(4) Intrinsic signal modulations can be measured from light reflectance alone; eliminating the need for extrinsic agents (e.g. voltage sensitive dyes and calcium indicators) that have not been widely used in non-human primates.

We conducted our testing in a macaque monkey performing an instructed reach-to-grasp task. Chronically implanted optical chambers provided access to M1 and S1 for ISOI during task performance. We exploited the blood vessel patterns visible through the artificial dura to guide precise placement of microelectrodes for electrophysiological recordings and for ICMS. Co-registration of imaging results and microelectrode results indicated that ISOI successfully localized spatial clusters of neurons involved in sensorimotor control of the arm and hand.

2. Methods

2.1. Animal

Both left and right hemispheres were studied in one female macaque monkey (*Macaca radiata*). The animal was 6–8 years old during the course of the study and weighed 3.8–4.0 kg. All procedures were approved by the University of Pittsburgh and Vanderbilt University Animal Care and Use Committees and followed the guidelines of the National Institutes of Health guide for the care and use of laboratory animals.

2.2. Head post and recording chamber

Once the animal was habituated to the primate chair and the behavioral training environment, a head fixation device was surgically implanted into the occipital bone and caudal aspects of the parietal bone. After several months of training on a reach-to-grasp task, a chronic recording chamber (26 mm internal diameter) was implanted in the hemisphere opposite to the arm used in the reach-to-grasp task. In the same procedure, the dura was surgically resected and replaced with a transparent membrane (Chen et al., 2002; Ruiz et al., 2013) for access to M1 and S1. At the start of every imaging session, a clear acrylic plate was temporarily secured inside the chamber to dampen cortical pulsations and minimize the associated artifact.

2.3. Reach-to-grasp task

The animal was trained to perform a reach-to-grasp task while seated in a primate chair and head fixed. The apparatus consisted of a partitioned carousel that was mounted onto a stepper motor (e.g., Umilta et al., 2007). Each partition provided access to a single target-object and no more than one partition was visible to the animal during a trial. Target objects were attached to rods that constrained their motion to the vertical axis. Thus, the animal could lift the object straight up; grip release allowed the object to drop back into its starting position. An Arduino Uno board (www.arduino.cc) controlled all task related parameters and timing. The animal was tested on two conditions (Fig. 1).

1. Go condition. In a successful trial, the animal had to reach, grasp, lift, and hold a spherical object. Objects included a Large Sphere (25 mm diameter) to produce a power grip or Small Sphere (10 mm diameter) to motivate a precision grip. The carousel rotated between trials to present objects in the exact same location to

encourage the same reach trajectory. To initiate a trial, the animal placed each hand over a photocell embedded in the waist plate. After holding this position for 1000–1500 ms, a blue LED started blinking as a “Go” cue. The animal had a 2000 ms time window to reach, grasp and lift the target object ~30 mm from the start position, which turned the LED solid. After holding the target object in the lifted position for 500 ms, the LED extinguished instructing the animal to release the object and return its hand to the start position within 1500 ms. Maintaining the hand at the start position for 1000 ms triggered a low frequency tone and LED blinks for 4000 ms during which both hands had to remain in position. Successful completion of all steps resulted in a correct trial and delivery of juice reward immediately after the LED and tone extinguished (~9000 ms from trial initiation). Failure to complete any step within the allotted time window, or removal of the opposite hand from the waist plate, resulted in an incorrect trial. In this event, a high frequency tone was delivered for 4000 ms followed by a 7000 ms timeout in which the apparatus was unresponsive to the monkey’s actions.

2. Withhold condition. In a successful trial, both hands had to maintain the start position for a total of 8000–9500 ms. To initiate a trial, the animal placed each hand at the start position. After holding this position for 1000–1500 ms, a white LED was turned on as a “Withhold” cue. Maintaining both hands at the start position for an additional 3000–4000 ms triggered a low frequency tone and LED blinks for 4000 ms followed by juice reward. Removal of either hand from the start position at any point resulted in an incorrect trial and the same consequences described in the Go condition.

2.4. Intrinsic signal optical imaging

M1 and S1 were imaged on separate sessions using red illumination (630 nm wavelength). Camera frames (504 × 504 pixels) were captured (100 Hz) with a 12-bit Dalsa 1M60P camera and temporally binned (5 data frames/s). Imaging lasted for 6 s/trial for a total of 30 data frames/trial. Imaging parameters and acquisition were controlled with an Imager 3001 system (Optical Imaging Ltd, Rehovot, Israel). Tandem lenses provided a 14 × 14 mm field-of-view (FOV), but images were cropped during post-processing to exclude edge artifacts and prominent blood vessels. Image acquisition was triggered on reach onset in the Large Sphere/Go condition and on cue onset in the Withhold condition (Fig. 1). The two conditions were presented in a pseudorandom order. In every imaging session, the animal completed 50–70 correct trials/condition. Inter-trial interval was ≥10 s.

Images acquired from successful trials were analyzed with MATLAB (Mathworks, Natick, MA) scripts. Motion correction was applied in the x- and y- dimensions to align all data frames to a single reference frame. Data frames were excluded from further analyses in the event of shifts >10 pixels (~278 μm) in a single dimension. Individual trials were then inspected frame-by-frame for quality. Trials were excluded from further analysis if they contained artifacts from LED instability, lens flares, and cerebrospinal fluid drifting in the field-of-view. Approximately 18 ± 8 % of trials (mean ± SEM) were excluded from each session.

To increase signal-to-noise ratio, the first data frame of each trial was subtracted from each subsequent data frame in the same trial. Next, frames were averaged as follows:

$$\text{Mean}F_i = \left[\left(F_{i,j=1} - F_{1,j=1}\right) + \left(F_{i,j=2} - F_{1,j=2}\right) + \left(F_{i,j=3} - F_{1,j=3}\right) + \ldots\left(F_{i,j=n} - F_{1,j=n}\right)\right]/n$$

F = single data frame (5 data frames/s), i = frame number within a trial (30 frames per trial), j = trial number within imaging run, F_1 = first frame, n = total number of trials in an imaging run. Every average frame was convolved with median and Gaussian filters to reduce low and high spatial frequency noise, respectively.

2.5. Vibrotactile stimulation

To our knowledge, at the time of the study, only one report had been published on the use of ISOI for assaying cortical activity during forelimb movements in primates (Heider and Siegel, 2014). This motivated us to include a well-established stimulus paradigm for benchmarking our ISOI results. We chose vibrotactile stimulation of focal points on the hand because it had been successfully used in identifying punctate spatial domains in monkey somatosensory cortex (Chen et al., 2001; Shoham and Grinvald, 2001; Friedman et al., 2008).

The forearm and hand were restrained in neutral position. Probes (2 mm diameter) attached to piezoceramic benders (Noliac North America, Alpharetta, GA) mechanically stimulated the glabrous side of the hand (Friedman et al., 2011). Four locations (distal D1, distal D2, proximal D3, and distal thenar) were stimulated on separate trials. Each stimulation trial consisted of a 3 s train of pulses (8 Hz pulse frequency, 20 ms pulse width). Stimulation parameters were controlled with a pair of Grass Instruments stimulators (Model S88 Dual Output; Artisan Technology Group, Champaign, IL). Each pulse indented the skin ~250 μm. An imaging trial lasted for 5 s and the stimulation train started after 2 data frames of baseline activity. During Blank trials the probes contacted the skin, but the benders were not actuated.

2.6. Single unit recording

We recorded single unit activity in domains that we imaged in M1 and S1. Our objective was to determine how single units within these domains modulated their activity in the reach-to-grasp task. A customized 3-axis microdrive was attached to the recording chamber to advance a tungsten microelectrode (0.5–1.0 MΩ impedance; Microprobes, Gaithersburg, MD) through the artificial membrane and into cortex (Arieli et al., 2002; Ruiz et al., 2013). A surgical microscope aided visualization of blood vessel patterns, which served as landmarks for microelectrode positioning. Signals were bandpass filtered (300–7500 Hz), amplified, and recorded (40 kHz sampling rate, 12-bit resolution) with Plexon Map Data Acquisition System (Plexon Inc. Dallas, TX). Single units were isolated during recording and further sorted with Offline Sorter (V3.3.5, Plexon Inc. Dallas, TX).

A single unit was considered a single neuron and included in the present analysis if three criteria were met. (1) Incidence of inter-spike-intervals ≤1 ms amounted to <0.5% of all

spikes recorded for that unit. (2) Peak-to-trough amplitude of the average waveform was ≥5x the amplitude of background activity. (3) Unit activity was recorded for ≥30 correct trials/condition. We were able to collect more trials/session with single unit recording as compared to ISOI. To capitalize on the larger number of trials, we expanded the Go condition to include a Large Sphere object (power grip) and a Small Sphere object (precision grip) during these recording sessions.

2.7. Intracortical microstimulation

We used intracortical microstimulation (ICMS) to map the motor representations that overlapped the domains that we imaged in M1. During ICMS the animal was awake, head-fixed, and still. Most ICMS sites were tested in the same microelectrode tracks that were used for neural recordings. Microelectrode depths were adjusted to target the approximate location of layer 5 (~1800 μm from cortical surface). Stimulation trains (60 ms duration, 300 Hz pulse frequency, 0.2 ms cathodal pulses) were generated from a Grass Stimulator (Model S88 Dual Output) and delivered at 1 Hz. Current amplitude was controlled with a Biphasic Stimulus Isolator (Bak Electronics Inc, Umatilla, FL) and increased from 0 μA until a movement was reliably evoked and characterized (max 100 μA). Current threshold was defined as the current intensity at which ICMS evoked movement on 50% of stimulation trains. At the end of ICMS, impedance of the tungsten microelectrode was relatively unchanged from the starting point (0.5–1.0 MΩ).

2.8. Somatosensory receptive field mapping

We recorded multi-unit activity from microelectrode penetrations throughout the postcentral gyrus for the purpose of mapping receptive fields. Our objective was to determine the relationship between the spatial domains identified with ISOI and the cutaneous representations of the arm and hand. The monkey was awake and head-fixed during the recordings. Each microelectrode penetration targeted the approximate depth of layer 4 (700–900 μm from cortical surface). Recordings here were conducted with the same system and filtering parameters used for measuring single unit activity during task performance. Signals were broadcasted over a loudspeaker for evaluating neural modulation in response to light skin stimulation and receptive field characterization. Sites that required intense stimulation (e.g. skin tapping), joint manipulation, or muscle palpation were classified as having deep receptors. Receptive fields were recorded on templates of line drawings of the body. Size, responsivity, and somatotopy of the receptive field at each recording site guided our estimation of borders between areas 1, 2, and 5 (Pons et al., 1985; Seelke et al., 2012).

2.9. Study timeline

The animal was trained for several months to perform the reach-to-grasp task. Performance was considered stable once the animal achieved 75% correct trials per session on 10 consecutive days (1 session/day). At that point an optical imaging chamber was implanted in the hemisphere opposite to the forelimb used in the reach-to-grasp task. After one week of recovery, daily sessions of the task resumed. M1 and S1 were studied with ISOI on alternate days. Next, we recorded single unit activity from the same M1 and S1 territories that were studied with ISOI. In addition, we mapped the motor and somatosensory representations of the forelimb in M1 and S1, respectively. Experimentation in this hemisphere concluded once

dural growth thickened to the extent of obscuring blood vessels as reliable landmarks for microelectrode placement (~70 days). At that point the animal was trained to perform the reach-to-grasp task with the opposite forelimb. The same data acquisition procedures were repeated in the hemisphere contralateral to that forelimb (~90 days). In addition, activity was measured in somatosensory cortex with ISOI during vibrotactile stimulation.

2.10. Experimental design and statistical analyses

Firing rates were analyzed for each single unit independently. A single unit was considered task-related if an ANOVA on the firing rates recorded in the three task conditions: Large Sphere/Go, Small Sphere/Go, and Withhold showed significant differences ($p<0.05$). Post hoc tests (Bonferroni corrected for 3 comparisons) were then carried out for each task-related unit. Firing rates were considered significantly different between task conditions if $p<0.01$. A separate analysis was conducted on task-related units to determine if they fired differentially during specific task phases. Thus, every trial was subdivided into 4 phases (280 ms/phase): (1) Pre-movement, (2) Reach, (3) Grasp, and (4) Withdrawal. Trials from the Large Sphere/Go and Small Sphere/Go conditions were pooled into a single Go condition. A single unit was considered tuned to task phase if an ANOVA on the firing rates in the 4 task phases showed significant differences ($p<0.05$). Post hoc tests (Bonferroni corrected for 6 comparisons) were then used to determine the task phase(s) with the highest firing rates ($p<0.008$).

3. Results

A macaque monkey performed a reach-to-grasp task with Go and Withhold conditions (Fig. 1). We measured activity in M1 and S1 using intrinsic signal optical imaging (ISOI) and single-unit recordings. To relate M1 activity patterns to forelimb somatotopy, we used intracortical microstimulation (ICMS) to map the motor representations in the same M1 territory. Similarly, to relate S1 activity to forelimb somatotopy, we mapped receptive fields with multi-unit recordings in microelectrode penetrations throughout the same S1 territory.

ISOI domains.

Neural activity drives a hemodynamic response that is measurable from the change in reflectance of red light illumination (630 nm wavelength). In that context, negative reflectance (i.e., pixel darkening) is a lagging indicator of increased neural activity. Accordingly, we consider clusters of darkened pixels as particularly relevant to our objective of surveilling the neocortex for “hot zones” of neural activity that support movement. We use the term *domain* to refer to spatial clusters of darkened pixels. In sensory cortex, *domains* (e.g., orientation domains, color domains in V1, V2, and V4) are defined as functional units whose neuronal population are not functionally identical but on average exhibit a preference or bias. These coherent responses have been visualized using multiple methods, including electrophysiology (e.g. Hubel and Wiesel, 1977), 2-deoxyglucose (e.g. Tootell et al., 1988), optical imaging (e.g., Blasdel and Salama, 1986; Grinvald et al., 1986), and high spatial resolution fMRI methods (e.g., Cheng, 2018).

3.1. Reach-to-grasp activates domains in M1 arm and hand representations

M1 hand domains.—This part of the study involved the left hemisphere and the right arm/hand. The field-of-view (FOV) was centered on the precentral gyrus over the expected location of the M1 hand representation (Fig. 2A, yellow rectangle). We hypothesized that negative reflectance would increase (i.e., pixels darken) in the Go condition, but that reflectance would remain relatively unchanged in the Withhold condition.

Negative reflectance did not increase during movement phases of the Go condition (i.e., Reach, Grasp, and Withdrawal). This was evident from the predominantly gray appearance of the optical images captured in the initial ~3 s from reach onset (Fig. 2B and G). Beyond that time point, pixels started to darken and peaked in intensity 4.6–5.0 s from reach onset. Dark pixels clustered into a large domain and two smaller domains (Fig. 2C, yellow outlines). Because pixel darkening is a surrogate for increased neural activity, we were motivated to determine the location of the domains with respect to the motor map. Thus, we placed several microelectrode penetrations in the larger domain and delivered ICMS to evoke a motor response. We found that this domain overlapped with digit and wrist sites (Fig. 2D, red and yellow dots), which means that it was in the M1 hand representation. ICMS sites did not extend as far rostral as the other two domains near the expected M1/dorsal premotor cortex (PMd) border. Nevertheless, the medio-lateral alignment of both domains with digit and wrist sites suggests that they were likely in the M1 hand representation. We therefore refer to the present constellation of domains as *M1 hand domains*.

Time courses of M1 hand domains.—It is well-established from ISOI in sensory cortex that stimulus onset leads to gradual pixel darkening that peaks within 2–3 s (Frostig et al., 1990; Chen-Bee et al., 2007; Sirotin et al., 2009). Our objective here was to understand how the temporal development of M1 hand domains compares to intrinsic signal time courses from previous work. So we placed two regions-of-interest (ROIs) over two of the M1 hand domains (Fig. 2E, blue and cyan ellipses). A third ROI served as a control and was purposely placed to avoid the M1 hand domains (Fig. 2E, orange). Time course profiles were similar for the cyan and blue ROIs (Fig. 2F, cyan and blue solid lines). First, both time courses showed a positive peak (i.e., pixel brightening) 2–3 s from reach onset. We did not expect any time courses to start with positive reflectance change as intrinsic signal time courses typically start with negative reflectance change. Nevertheless, the present time courses eventually became negative (~2.5 s for cyan and ~3.5 s for blue) and peaked 4.6–5.0 s from reach onset. The magnitude of the negative peak (−0.08 to −0.12%) was comparable to values from sensory cortical areas. In contrast, in the control ROI (Fig. 2E, orange solid line), only a limited change from baseline was observed and it was mostly positive. Thus, the three time course profiles described here indicate that pixel darkening peaked 4.6–5.0 s from reach onset and that this response was localized to punctate domains.

The same ROIs were used for measuring reflectance change during the Withhold condition. In the blue and cyan ROIs, time courses had positive values only (Fig. 2F, blue and cyan dashed lines). The magnitude of the positive peak for the cyan ROI was comparable to the magnitude of the negative peak achieved in the Go Condition. Even though negative

reflectance was detected in the control ROI (Fig. 2E, orange dashed line), it was considerably different from the time courses of domain activation. Specifically, negative peaks were larger and occurred later as shown in the cyan and blue ROIs in the Go condition. Next, we examined the optical maps frame-by-frame to visualize spatio-temporal differences in reflectance change between the Go and Withhold conditions (Fig. 2G and 2H, respectively). It was apparent from both conditions that M1 domains developed gradually over successive frames and darkened in the Go condition only. These observations support the likelihood that movement-related activity in M1 (i.e., spiking and/or LFP) was responsible for domain darkening observed in the Go condition. Domain brightening in the Withhold condition is less straightforward and potential interpretations are explored in the Discussion. Nevertheless, lack of darkening indicates that there was no increase in neural activity.

M1 arm domain.—To examine whether ISOI can detect activation in other zones of the forelimb representation, we centered the FOV more medially over the expected location of the M1 arm representation (Fig. 3A, yellow rectangle). This part of the study involved the right hemisphere and the left arm/hand. Consistent with our observations in the M1 hand representation, negative reflectance did not increase in the initial ~3 s from reach onset (Fig. 3B). Negative reflectance increased beyond this time point and a relatively large domain became apparent 5–6 s after reach onset (Fig. 3C, yellow outline). This domain mostly overlapped ICMS sites that evoked shoulder and elbow movements (Fig. 3D, white and green dots). Wrist and digit movements were evoked only from sites near the lateral edge of this domain. Accordingly, we refer to the present domain as *M1 arm domain*.

Time courses of M1 arm domain.—We defined two ROIs for the arm domain (Fig. 3E, cyan and blue ellipses). Including a control ROI was not feasible because the domain occupied most of the field-of-view. Time courses here were generally similar to the time courses measured from the M1 hand domains (Fig. 2F). In the Go condition, time courses from both ROIs were initially positive-going (Fig. 3D, cyan and blue solid lines) then became negative ~3 s from reach onset. The increase in negative reflectance continued until the final imaging frame (6 s from reach onset), but it would have likely peaked at that point given the magnitude of reflectance change (−0.15%). In contrast, no negative reflectance was measured from either ROI in the Withhold condition (Fig. 3F, cyan and blue broken lines). The near overlap between time courses from the two ROIs supports the likelihood that they were both in the same domain. Time course profiles also indicate that the domain was activated in the Go condition only. A side-by-side comparison of a series of optical images is instructive for visualizing spatio-temporal differences between the Go and Withhold conditions (Fig. 3G and H). Gradual development of the domain in the Go condition and pixel brightening in the Withhold condition were both consistent with our observations in M1 hand domains.

3.2. M1 domains contain single units that encode reaching and grasping

We recorded single unit activity from the M1 domains. The motivation behind these recordings was to assay spiking activity that likely contributed to domain activation. Given the profile of reflectance change in the Go and Withhold conditions, we hypothesized that

firing rates would increase during movement in the Go condition and decrease or remain the same in the Withhold condition. We also hypothesized that units in M1 hand domains would preferentially encode hand movements associated with grasping, whereas units in the M1 arm domain would preferentially encode arm movements associated with reaching and withdrawal.

Two objects were tested in the Go condition. (1) Large Sphere; gripped with five digits (power grip). (2) Small sphere; gripped with digits 1, 2, and 3 (precision grip). A total of 40 single units were recorded from 22 penetrations in M1. A single unit was considered task-related if a comparison (ANOVA) of firing rates in the Large Sphere/Go, Small Sphere/Go, and Withhold conditions showed significant differences ($p<0.05$). We found that 38/40 (95%) units were task-related. In follow up comparisons on the task-related units (Bonferroni, $p<0.01$), we found that 34/38 (89%) units fired at higher rates in the Large Sphere/Go condition as compared to the Withhold condition. Similarly, 34/38 (89%) units fired at higher rates in the Small Sphere/Go condition as compared to the Withhold condition. Thus, most units fired at higher rates in the Go condition, irrespective of object size, as compared to the Withhold condition. Only 5/38 units (13%) fired differentially between the Large Sphere/Go and Small Sphere/Go conditions. Two of these units were in M1 hand domains and three were in the M1 arm domain. That only a limited number of single units differentiated between the Large and Small Spheres could reflect similarities between prehension strategies used for both objects. The observation may also be due to the relatively small sample of units. Nevertheless, all task-related units fired at significantly higher rates (see experimental design) during one or more task phases: (1) pre-movement, (2) reach, (3) grasp, and (4) withdrawal. These units, and others like them, likely contributed to the domains that we found in M1 using ISOI.

Grasp units were defined as units that fired maximally during the *Grasp phase*. *Grasp units* accounted for the largest category 16/38 (42%) of task-related units in M1. Most of these units (12/16 units) were located in M1 hand domains (Fig. 4A, yellow symbols). Fig. 4B shows the peri-stimulus time histogram (PSTH) from a representative unit. Neural activity from the Go conditions was aligned to the start of object lifting, which occurred with grasp completion. In both Go conditions, firing rates started to increase with reach onset and peaked during object grasping (Fig. 4B). Firing rates started to return to baseline even while the hand was still holding and lifting the object (Fig. 4B, time zero). After pooling trials from both Go conditions, firing rate modulation in response to task phase was confirmed (ANOVA, $F(3,192) = 28.19$, $p<0.001$) and was highest for the *Grasp phase* (Bonferroni, $p<0.008$). In contrast, no modulation in neural activity was observed in the Withhold condition (Fig. 4B).

Reach units were defined as units that fired maximally during the *Reach phase*. *Reach units* accounted for 9/38 (24%) of task-related units. All of these units (9/9 units) were located in the M1 arm domain (Fig. 4D, cyan symbols). The PSTH from a representative *Reach unit* is plotted in Fig. 4E. In both Go conditions, firing rates started to increase hundreds of milliseconds before movement and peaked during reach onset. During object grasping, lifting, and holding (Fig. 4E, time zero) firing rates decayed to levels below those recorded in the Withhold condition. Activity started to increase again and peaked with the onset of

forelimb withdrawal (~0.6 s after grasp+lift). Thus, the bimodal peaks for this unit coincided with the arm transport phases of the task (i.e., reach and withdrawal). In contrast, grasp, lift and hold coincided with the low activity period in between the firing peaks. After pooling trials from both Go conditions, firing rate modulation in response to task phase was confirmed (ANOVA, $F(3,305) = 43.16$, $p < 0.001$) and was highest during the *Reach phase* (Bonferroni, $p<0.008$).

Both units were defined as units that fired at rates that were statistically indistinguishable (i.e., Bonferroni, $p>0.01$) during the *Reach phase* and *Grasp phase.* These units accounted for 9/38 (24%) of the task-related units and were distributed equally between the M1 hand domains and the M1 arm domain (Fig. 4A and D, red symbols).

Neither units.—Two types of units were included here. First, units that fired preferentially in the *Withdrawal phase* alone ($n= 2$). Second, units that suppressed their firing rates below baseline throughout all phases of the task ($n=2$). All of these units were located in the M1 arm domain and accounted for 4/38 (11%) of task-related units in M1.

3.3. Population response in M1 domains

We investigated the population response for units recorded in the M1 hand domains and separately for units recorded in the M1 arm domain. Firing rates were normalized for all trials recorded from a given unit (highest firing rate = 1; lowest firing rate = 0). Normalization ensured that variability from unit-to-unit in baseline firing rates did not influence the population response.

M1 hand domains.—The population response for the M1 hand domains was calculated from the 18 single units (Fig. 4C, pie chart) recorded in that territory. The population PSTH had a similar profile for the large and small objects (Fig. 4C). Population activity started to increase before movement onset and peaked during the *Grasp phase*. Activity started to decline once the object was grasped and lifting started. In contrast, there was no modulation in the Withhold condition. Thus, the population response here supports the likelihood that spiking during the *Grasp phase* was an important driver of the negative reflectance that we observed with ISOI in the M1 hand domains.

M1 arm domain.—The population response for the M1 arm domain was calculated from the 22 single units (Fig. 4F, pie chart) recorded in that territory (Fig. 4F). Population activity started to increase before movement and peaked during reach onset. Activity levels declined rapidly during the *Grasp phase* and approached levels recorded in the Withhold condition. Activity increased again during the *Withdrawal phase* (~0.6 s after lift), but not to the levels recorded during the *Reach phase*. Thus, the population response recorded here supports the likelihood that spiking during the *Reach* and the *Withdrawal phases* drove the negative reflectance that we observed with ISOI in the M1 arm domain. Spiking related to the *Grasp phase* cannot be ruled out, but the PSTH peaks were clearly aligned with the arm transport phases.

3.4. Reach-to-grasp activates domain in S1 hand representations

S1 domain.—This part of the study involved the left hemisphere and the right arm/hand. The FOV was centered on the postcentral gyrus over the expected locations of the somatosensory hand representations in areas 1 and 2 (Fig. 5A). We hypothesized that negative reflectance would increase in the Go condition due to hand contact with the target object, but that reflectance would remain relatively unchanged in the Withhold condition. Similar to our observations in M1, negative reflectance did not increase in the initial ~3.0 s from reach onset (Fig. 5B). From this point onwards, negative reflectance increased within a domain that peaked in size and intensity by ~5.0 s from reach onset (Fig. 5C, yellow outline). Microelectrode mapping of receptive fields showed that the present domain overlapped primarily with cutaneous representations of digits 2–5 in area 2 (Fig. 5D).

Time courses of the S1 domain.—We examined the temporal development of the S1 domain. Our objective was to understand how time course profiles here would compare to the time course profiles that we observed in M1. We placed two ROIs in the S1 domain (Fig. 5E, cyan and blue ellipses) and a third ROI in a control location (Fig. 5E, orange). In the Go condition, time courses from both cyan and blue ROIs were initially positive-going and peaked 2–3 s after reach onset (Fig. 5F, cyan and blue solid lines). Time courses entered negative territory ~3 s from reach onset and then peaked by ~5 s. In contrast, the time course from the control ROI was always positive and deviated only minimally from baseline (Fig. 5F, orange solid line). Thus, the three time course profiles indicate that negative reflectance occurred in the Go condition only, peaked ~5 s from reach onset, and was spatially confined to a domain. The present time course profiles are therefore similar to the time course profiles that we reported for the M1 domains.

In the Withhold condition, time courses were positive in all three ROIs (Fig. 2F, dashed lines). Time courses from the cyan and blue ROIs nearly overlapped and had an overall higher magnitude than the time course measured from the orange ROI. The positive-going time courses in the Withhold condition support the likelihood that negative reflectance in the Go condition was related to movement execution. It is evident from the frame-by-frame comparison that the S1 domain develops gradually in the Go condition and that there is no pixel-darkening in the Withhold condition (Fig. 5G and H, respectively).

We imaged a similar field-of-view in the right hemisphere (Fig. 6A) while the monkey performed the task with the left arm/hand. The S1 domain was somewhat less focal here as compared to the left hemisphere. Nevertheless, temporal onset in relation to movement (Fig. 6B–D) was comparable between the present S1 domain and the counterpart in the left hemisphere (Fig. 5G). Microelectrode mapping of receptive fields confirmed that the present S1 domain overlapped with the somatosensory representations of the digits and the palm (Fig. 6E). Thus, ISOI results from S1 were consistent between both hemispheres.

3.5. S1 domain contains single units that encode object contact

Our next objective was to assay the spiking activity that could have driven the S1 domain. We hypothesized that task-related units would fire maximally during hand contact with the target object in the Go conditions. We recorded 22 single units from 12 microelectrode

tracks. Recordings were conducted in the right hemisphere while the monkey performed the reach-to-grasp task with the left arm/hand. We found that 20/22 (91%) units were task-related (ANOVA, $p<0.05$). Follow up comparisons on the task-related units (Bonferroni, $p<0.01$) showed that 13/20 (65%) units fired at higher rates in the Large Sphere/Go condition as compared to the Withhold condition. Similarly, 14/20 (70%) units fired at higher rates in the Small Sphere/Go condition as compared to the Withhold condition. Also, 12/20 units (60%) fired differentially for the small and large objects.

Next, we examined whether task-related units fired preferentially for task phases. We found that 18/20 (90%) units fired differentially (ANOVA, $p<0.05$) across task phases. *Grasp units* accounted for 14/20 (70%) of task-related units and they were present throughout the S1 domain (Fig. 6F, yellow symbols). *Reach units* accounted for only 2/20 (10%) of task-related units (Fig. 6F, cyan symbols). The only *Both unit* was recorded on the same microelectrode track as a G*rasp unit* (Fig. 6F, red symbol). *Neither units* accounted for 3/20 (15%) of task-related units (Fig. 6F, gray symbol).

3.6. Population response in S1 domains

The normalized population response was calculated from the 22 recorded units (Fig. 6G, pie chart). The population PSTH was nearly overlapped for the large and small objects (Fig. 6G). Firing rates were largely unchanged before movement and even into reach onset. Firing rates then increased sharply and peaked during object grasping (Fig. 6G, immediately before time zero). Activity began to decline just before object lifting started (Fig. 6G, time zero) and approached levels recorded in the Withhold condition. A brief and relatively small burst of activity occurred at the end of forelimb withdrawal when the hand contacted the waist plate to return to the start position. Thus, the population PSTH suggests that spiking related to object handling was likely the primary diver of the negative reflectance that we observed with ISOI in the S1 domain.

3.7. Vibrotactile stimulation activates focal S1 domains

We had two objectives that we believe could be addressed with ISOI in response to passive stimulation of the hand. First, determine whether our ISOI paradigm was sensitive enough to detect focal domains. Second, determine whether we can drive negative reflectance at time courses that are on par with previous work (i.e., negative peak 2–3 from stimulation onset). We imaged the same FOV as in Fig. 6 and restrained the contralateral forelimb for passive stimulation. Vibrotactile stimulation was delivered with 2 mm diameter probes to sites on the glabrous side of the hand. We hypothesized that domains specific to each vibrotactile site would spatially coincide with the matching zone from the receptive field map.

Focal S1 domains.—We tested four sites including proximal digit 3, distal digit 2, distal digit 1, and distal thenar (Fig. 7F, hand). Activation domains became apparent for each condition after subtraction of the blank condition (i.e., no stimulation) or another vibrotactile condition. A similar image subtraction strategy has been used to reveal digit domains in primate somatosensory cortex (Chen et al., 2001; Friedman et al., 2008) and is essential for defining functional domains in visual cortex (e.g., Lu and Roe, 2007, 2008). Fig. 7A–D shows the activation domains for the four vibrotactile sites. Each domain was focal (1.0–2.5

mm^2) and corresponded closely with matching receptive fields (Fig. 7E). These results confirm that our ISOI paradigm can indeed resolve focal domains even when they are adjacent to one another.

Time courses of the S1 domains.—Time courses were measured from ROIs (not shown) that were centered onto each domain. Time courses were negative-going from the outset and peaked within 2–3 s of stimulation onset (Fig. 7F, solid lines). In contrast, in the condition with no stimulation, time courses were either positive or hovered near baseline (Fig. 7F, dashed lines). The present time courses are consistent with previous ISOI studies in several sensory modalities including macaque S1 in response to mechanical stimulation of the digits (Shoham and Grinvald, 2001). Importantly, the profile of time courses recorded in the present stimulation conditions differed from the profile of time courses that we measured in M1 and S1 during the Go condition (Figs. 2F, 3F, and 5F). There we observed a small positive peak (2–3 s from reach onset) followed by a large negative peak (~5 s from reach onset).

4. Discussion

We successfully used intrinsic signal optical imaging (ISOI) to localize functional domains that were active in M1 and S1 during reaching and grasping. Domains in M1 and S1 overlapped the arm and hand representations. Single unit recordings from within the domains indicated that firing rates were modulated during reaching, grasping, or both phases. Our study provides proof-of-concept that ISOI can be used to measure cortical activity during motor behavior in non-human primates.

4.1. Why imaging?

The spatial continuity possible with optical imaging confers a critical advantage for assaying cortical activity. Sampling would be considered comparatively sparse with microelectrode arrays as these devices are limited by inter-shank distance and by packing density of multiple arrays. Despite the potential for outstanding spatial sampling, imaging techniques have been used in only a few non-human primate studies of forelimb control. At the level of brain areas, fMRI was used in behaving macaque monkeys to localize the constituent zones of the parietal-frontal network involved in reaching and grasping (Nelissen and Vanduffel, 2011). At the cellular level, two-photon imaging was used in marmosets to identify populations of M1 neurons active during reaching and grasping (Kondo et al., 2018) and in an arm control task (Ebina et al., 2018). All of these studies represent fundamental advances in the application of imaging tools towards understanding cortical control of movement in primates. However, ISOI opens a new and valuable possibility for mesoscale imaging (i.e., wider than two-photon), at high spatial resolution (i.e., higher than fMRI), in behaving macaques. Moreover, compatibility of the present optical window with fMRI and with two-photon imaging means that the strengths of ISOI could be coupled with other imaging modalities and with electrophysiological recordings. For example, activation domains could be first localized with ISOI then individual neurons can be interrogated with two-photon imaging.

4.2. Size and time course of reach-to-grasp domains

The M1 and S1 domains that we imaged in the reach-to-grasp task were large as compared to the focal domains that have been reported in primate visual cortex (e.g. Frostig et al., 1990; Lu and Roe, 2007) and somatosensory cortex (Chen et al., 2001; Shoham and Grinvald, 2001; Friedman et al., 2008). Our experiment with passive stimulation to the hand confirmed that our imaging paradigm has the capacity for detecting focal domains. Thus, the relatively large domains that we reported for the reach-to-grasp task likely reflect real differences in cortical activation that supports arm and hand movements as compared to cortical activation in response to focal mechanical stimulation. Relatively large domains in M1 suggest that many arm and hand muscles are co-activated during reaching and grasping. This coupled with the point spread of intrinsic signals (Frostig et al., 2017) could have blurred multiple focal domains into seemingly large domains. Similarly, contact between multiple digits and the target could have led to the co-activation of contiguous S1 domains and the impression of a large activation domain. It is also important to note that extended training on the reach-to-grasp task could have reduced attention and effort, leading to decreases in metabolic demands (e.g. Tanigawa et al., 2010; Picard et al., 2013) and potentially altering domain dimensions.

Time courses measured from M1 and S1 domains confirmed that increased negative reflectance (i.e., pixel darkening) occurred in the Go condition only. The time course profiles for those domains indicated that intrinsic signal modulation in response to the reach-to-grasp task differed from time courses reported for sensory cortical areas in response to passive stimulation. In the reach-to-grasp task we observed an initial increase in positive reflectance (i.e., pixel brightening) followed by a considerably larger increase in negative reflectance. The negative peak was not achieved until ~5 s from reach onset. In contrast, passive stimulation has been shown to drive a triphasic time course that starts with an increase in negative reflectance that peaks 2–3 s from stimulation onset (e.g., Frostig et al., 1990; Chen-Bee et al., 2007; Sirotin et al., 2009). We observed similar time courses in our own passive stimulation experiment. It is therefore unlikely that our imaging paradigm contributed to the unexpected time courses that we observed in the reach-to-grasp task. A potential explanation for the late timing of the negative peak is that it was delayed due to the preceding positive reflectance (2–3 s). This unexpected positive reflectance could have been a lagging indicator of neural activity suppression. However, this explanation seems unlikely given that the Withhold condition largely involved positive reflectance without change in single unit activity. An alternative explanation is that the positive reflectance in the Go condition was due to complex hemodynamics that were not captured in our imaging sequence. For example, it could have been related to reflectance change that started in one trial, continued into the inter-trial interval, and then encroached into the next trial. Our inter-trial interval (≥10 s) should have safeguarded against this potential complication, but we cannot rule out the possibility that signals may not have returned to baseline at the start of each trial. Nevertheless, previous work has shown that stimulus onset drives negative reflectance even if it is delivered during positive reflectance (Chen-Bee et al., 2010). It is therefore unlikely that out inter-trial interval was a factor in the observed positive reflectance. Another possibility is that the unexpected positive reflectance reveals an anticipatory hemodynamic response in the reach-to-grasp task. Thus, the initial positive reflectance could be an

indication of changes in blood vessels or in blood gases that preempted the hemodynamic response that ensued from increased neural activity.

4.3. M1 domains encode reaching and grasping

ISOI revealed at least two regions of activation in M1 during reaching and grasping. The medial region included a relatively large domain that overlapped part of the arm representation (shoulder/elbow). In contrast, the lateral region included three focal domains that overlapped part of the hand representation (wrist/digits). We assayed single unit activity from within the hand and arm domains. Although the sample of units was relatively small, it still provided insight about the spiking activity that likely activated the domains. The population of units in the M1 hand domains fired maximally during the *Grasp phase*. In contrast, the population of units recorded from the M1 arm domain fired maximally during reaching and withdrawal. These two population profiles were likely shaped from the spatial clustering of Grasp units in the M1 hand domains and Reach units in the M1 arm domain. The results collectively suggest that the M1 hand domains may be "hot zones" for encoding grasping and other manual behaviors. Similarly, the M1 arm domain may be a "hot zone" for encoding arm transport and other arm movements. A more complete understanding of the encoding properties of the domains requires a larger sample of single units from within the domains as well as assaying single units from outside of the domains. Nevertheless, our limited sample of single units indicates that a strict medio-lateral division of function between the domains is unlikely for several reasons. First, *Both Units,* which fired at comparable rates during both *Reach* and *Grasp phases,* were equally distributed between the arm and hand domains. Second, *Grasp Units* were present in the M1 arm domain, albeit in fewer numbers than *Reach Units*. Third, firing rates for *Grasp Units* started to increase during the *Reach phase*.

4.4. Functional clustering in M1

Our results suggest that M1 domains may be endowed with functional clustering and with functional intermingling. Two studies that examined reaching and grasping in monkeys are particularly relevant here because they documented the spatial locations of the recorded units with respect to each other and to the motor map. In a behavioral paradigm similar to our task, Saleh et al., 2012 reported spatial intermingling of reach units, grasp units, and reach/grasp units in M1 on the precentral gyrus. The lack of spatial clustering of unit classes was presumed to be at least in part related to recording sites overlapping the M1 zone with mixed representations of the arm and hand (Park et al., 2001). Thus, clusters of reach units or grasp units could have existed elsewhere in the forelimb representation; perhaps beyond the implanted microelectrode array. Rouse & Schieber (2016) sampled neural activity from the entire medio-lateral extent of the M1 forelimb representation in the bank of the central sulcus. In that study, units recorded from the arm representation encoded target location (i.e., reach direction) preferentially over target object (i.e., grip posture). In contrast, units recorded from the hand representation encoded the target object preferentially over reach direction. Nevertheless, this functional clustering was outweighed by the fact that encoding of reach direction and grip posture was co-extensive in the forelimb representation. Thus, from our perspective, whether the encoding of reaching and grasping in M1 is more

clustered or more intermingled, remains unanswered. The issue cannot be resolved with our limited sample of single units.

Although prevalent in sensory cortical areas, evidence for functional clustering in M1 is by comparison scarce. The discrepancy could be related to differences in the neural circuitry of sensory cortical areas (e.g., prominent layer 4 and orderly maps) as compared to M1. However, it is also possible that detection of functional clustering is more straightforward in sensory cortex where stimuli can be tightly controlled and imaging methods have been exploited for decades. Indeed, when both of these provisions have been met, functional clustering has been reported in M1. For example, fMRI studies have shown somatotopic organization in M1 of individual fingers in humans performing a finger tapping task (Ejaz et al., 2015; Huber et al., 2020). In contrast, somatotopy was considered absent for the M1 digit representations when mapped with microelectrode recordings in the central sulcus of macaques (Schieber and Hibbard, 1993). More diverse and complex behaviors have been shown to cluster in mouse M1 with 2-photon imaging (Dombeck et al., 2009; Wang et al., 2017). Similarly, ICMS trains in monkeys evoke specific behaviors from discrete M1 zones that could be considered functional clusters (e.g., Graziano et al., 2002; Stepniewska et al., 2014; Adelsberger et al., 2014). Moreover, each cluster is preferentially connected within M1 to a constellation of functionally-matching zones (Card and Gharbawie, 2020). Thus, as an organizing principle in M1, functional clustering appears to be conserved across species and is readily reveled using several techniques.

4.5. ISOI domains in S1

The spatial domain activated in somatosensory areas 1 and 2 during the reach-to-grasp task overlapped with the representations of digits 2–5 and the palm. The location of this domain is consistent with zones where long-train (500 ms) ICMS has been shown to evoke digits movements that closely resemble grasping Baldwin et al., 2018; Gharbawie et al., 2011. Imaging more medially during task performance showed little/no activity in the forearm representations, which suggests that hand-object contact was the primary driver of negative reflectance. Indeed, this was confirmed with single unit recordings, which showed that the S1 domain was enriched with units that fired maximally once the hand grasped the target object. The rapid decline in the population response, even while the hand was still grasping the object, suggests that the spikes recorded may be primarily attributed to rapidly adapting receptors. Similar response profiles have been reported for “Contact-tuned” and “Contact-grasp” neurons (Gardner et al., 2006), which collectively accounted for ~32% of units recorded from S1 in a reach-to-grasp task similar to the one used here.

4.6. Conclusion

Our study confirms the feasibility of ISOI – a mesoscale optical imaging method - for measuring cortical activity that supports the control of arm and hand movements. ISOI can be used in conjunction with fMRI to zoom in on cortical areas of interest for imaging at higher spatial resolution. ISOI can also enhance two-photon imaging as the wide field-of-view from ISOI can efficiently localize “hot zones” of activity for directing the narrow field-of-view of two-photon imaging.

Acknowledgments

Funding

The project was supported by NIH R01 NS105697 (OAG), NIH K99/R00 NS079471 (OAG), Whitehall Foundation Inc. research grant 2017-12-94 (OAG), NIH R01 NS044375 (AWR, RMF), and NIH R01 NS093998 (AWR, RMF). The following funds to AWR from Chinese funding sources were NOT used to support this research: National Key R&D Program of China 2018YFA0701400, National Natural Science Foundation 31627802, Zhejiang Provincial Dept of Science & Technology 2020C03004, China NSFC-US NIH Cooperative Biomedical Grant NSFC Grant 8191101288. There is no overlap.

References

Adelsberger H, Zainos A, Alvarez M, Romo R, Konnerth A, 2014 Local domains of motor cortical activity revealed by fiber-optic calcium recordings in behaving nonhuman primates. Proc. Natl. Acad. Sci. USA 111, 463–468. [PubMed: 24344287]

Arieli A, Grinvald A, Slovin H, 2002 Dural substitute for long-term imaging of cortical activity in behaving monkeys and its clinical implications. J. Neurosci. Methods 114, 119–133. [PubMed: 11856563]

Baldwin MKL, Cooke DF, Goldring AB, Krubitzer L, 2018 Representations of fine digit movements in posterior and anterior parietal cortex revealed using long-train intracortical microstimulation in macaque monkeys. Cerebral Cortex 28, 4244–4263. doi: 10.1093/cercor/bhx279. [PubMed: 29136133]

Blasdel GG, Salama G, 1986 Voltage-sensitive dyes reveal a modular organization in monkey striate cortex. Nature 321, 579–585. [PubMed: 3713842]

Card NS, Gharbawie OA, 2020. Principles of intrinsic motor cortex connectivity in primates. J. Neurosci. 40, 4348–4362. [PubMed: 32327531]

Chen-Bee CH, Agoncillo T, Lay CC, Frostig RD, 2010 Intrinsic signal optical imaging of brain function using short stimulus delivery intervals. J. Neurosci. Methods 187, 171–182. [PubMed: 20079373]

Chen-Bee CH, Agoncillo T, Xiong Y, Frostig RD, 2007 The triphasic intrinsic signal: implications for functional imaging. J. Neurosci. 27, 4572–4586. [PubMed: 17460070]

Chen LM, Friedman RM, Ramsden BM, LaMotte RH, Roe AW, 2001 Fine-scale organization of SI (area 3b) in the squirrel monkey revealed with intrinsic optical imaging. J. Neurophysiol. 86, 3011–3029. [PubMed: 11731557]

Chen LM, Heider B, Williams G V, Healy FL, Ramsden BM, Roe AW, 2002 A chamber and artificial dura method for long-term optical imaging in the monkey. J. Neurosci. Methods 113, 41–49. [PubMed: 11741720]

Cheng K, 2018 Exploration of human visual cortex using high spatial resolution functional magnetic resonance imaging. Neuroimage 164, 4–9. [PubMed: 27845253]

Dombeck DA, Graziano MS, Tank DW (2009) Behavioral/systems/cognitive functional clustering of neurons in motor cortex determined by cellular resolution imaging in awake behaving mice.

Ebina T, Masamizu Y, Tanaka YR, Watakabe A, Hirakawa R, Hirayama Y, Hira R, Terada S-I, Koketsu D, Hikosaka K, Mizukami H, Nambu A, Sasaki E, Yamamori T, Matsuzaki M, 2018 Two-photon imaging of neuronal activity in motor cortex of marmosets during upper-limb movement tasks. Nat. Commun. 9, 1879. [PubMed: 29760466]

Ejaz N, Hamada M, Diedrichsen J, 2015 Hand use predicts the structure of representations in sensorimotor cortex. Nat. Neurosci. 18, 1034–1040. [PubMed: 26030847]

Fetz EE, Cheney PD, 1980 Postspike facilitation of forelimb muscle activity by primate corticomotoneuronal cells. J. Neurophysiol. 44, 751–772. [PubMed: 6253604]

Friedman RM, Chen LM, Roe AW, 2008 Responses of areas 3b and 1 in anesthetized squirrel monkeys to single- and dual-site stimulation of the digits. J. Neurophysiol. 100, 3185–3196. [PubMed: 18922955]

Friedman RM, Dillenburger BC, Wang F, Avison MJ, Gore JC, Roe AW, Chen LM, 2011 Methods for fine scale functional imaging of tactile motion in human and nonhuman primates. Open Neuroimaging J. 5, 160–171.

Frostig RD, Chen-Bee CH, Johnson BA, Jacobs NS, 2017 Imaging Cajal's neuronal avalanche: how wide-field optical imaging of the point-spread advanced the understanding of neocortical structure-function relationship. Neurophotonics 4, 031217. [PubMed: 28630879]

Frostig RD, Lieke EE, Ts'o DY, Grinvald A, 1990 Cortical functional architecture and local coupling between neuronal activity and the microcirculation revealed by in vivo high-resolution optical imaging of intrinsic signals. Proc. Natl. Acad. Sci. USA 87, 6082–6086. [PubMed: 2117272]

Gardner EP, Ro JY, Babu KS, Ghosh S, 2006 Neurophysiology of prehension. II. Response diversity in primary somatosensory (S-I) and motor (M-I) cortices. J. Neurophysiol. 97, 1656–1670. [PubMed: 17093113]

Georgopoulos AP, Schwartz AB, Kettner RE, 1986 Neuronal population coding of movement direction. Science 233, 1416–1419. [PubMed: 3749885]

Gharbawie OA, Stepniewska I, Qi H, Kaas JH, 2011 Multiple parietal-frontal pathways mediate grasping in macaque monkeys. J. Neurosci 31, 11660–11677. doi: 10.1523/JNEUROSCI.1777-11.2011. [PubMed: 21832196]

Graziano MSA, Taylor CSR, Moore T, 2002 Complex movements evoked by microstimulation of precentral cortex. Neuron 34, 841–851. [PubMed: 12062029]

Griffin DM, Hoffman DS, Strick PL, 2015 Corticomotoneuronal cells are "functionally tuned". Science 350, 667–670. [PubMed: 26542568]

Grinvald A, Frostig RD, Siegel RM, Bartfeld E, 1991 High-resolution optical imaging of functional brain architecture in the awake monkey. Proc. Natl. Acad. Sci. USA 88, 11559–11563. [PubMed: 1763070]

Grinvald A, Lieke E, Frostig RD, Gilbert CD, Wiesel TN, 1986 Functional architecture of cortex revealed by optical imaging of intrinsic signals. Nature 324, 361–364. [PubMed: 3785405]

Hatsopoulos NG, Xu Q, Amit Y, 2007 Encoding of movement fragments in the motor cortex. J. Neurosci. 27, 5105–5114. [PubMed: 17494696]

Heider B, Siegel RM, 2014 Optical imaging of visually guided reaching in macaque posterior parietal cortex. Brain Struct. Funct. 219, 495–509. [PubMed: 23392845]

Hubel DH, Wiesel TN, 1977 Ferrier lecture. Functional architecture of macaque monkey visual cortex. Proc. R. Soc. Lond. Ser. B, Biol Sci 198, 1–59. [PubMed: 20635]

Huber L, Finn ES, Handwerker DA, Bönstrup M, Glen DR, Kashyap S, Ivanov D, Petridou N, Marrett S, Goense J, Poser BA, Bandettini PA, 2020 Sub-millimeter fMRI reveals multiple topographical digit representations that form action maps in human motor cortex. Neuroimage 208, 116463. [PubMed: 31862526]

Kondo T, Saito R, Otaka M, Yoshino-Saito K, Yamanaka A, Yamamori T, Watakabe A, Mizukami H, Schnitzer MJ, Tanaka KF, Ushiba J, Okano H, 2018 Calcium transient dynamics of neural ensembles in the primary motor cortex of naturally behaving monkeys. Cell Rep. 24, 2191–2195. [PubMed: 30134178]

Kwan HC, MacKay WA, Murphy JT, Wong YC, 1978 Spatial organization of precentral cortex in awake primates. II. Motor outputs. J. Neurophysiol. 41, 1120–1131. [PubMed: 100584]

Lu HD, Chen G, Tanigawa H, Roe AW, 2010 A motion direction map in macaque V2. Neuron 68, 1002–1013. [PubMed: 21145011]

Lu HD, Roe AW, 2007 Optical imaging of contrast response in Macaque monkey V1 and V2. Cereb. Cortex 17, 2675–2695. [PubMed: 17264252]

Lu HD, Roe AW, 2008 Functional organization of color domains in V1 and V2 of macaque monkey revealed by optical imaging. Cereb. Cortex 18, 516–533. [PubMed: 17576751]

Moran DW, Schwartz AB, 1999 Motor cortical representation of speed and direction during reaching. J. Neurophysiol. 82, 2676–2692. [PubMed: 10561437]

Nelissen K, Vanduffel W, 2011 Grasping-related functional magnetic resonance imaging brain responses in the macaque monkey. J. Neurosci. 31, 8220–8229. [PubMed: 21632943]

Nelson RJ, Sur M, Felleman DJ, Kaas JH, 1980 Representations of the body surface in postcentral parietal cortex of Macaca fascicularis. J. Comput. Neurol. 192, 611–643.

Park MC, Belhaj-Saïf A, Gordon M, Cheney PD, 2001 Consistent features in the forelimb representation of primary motor cortex in rhesus macaques. J. Neurosci 21, 2784–2792. [PubMed: 11306630]

Picard N, Matsuzaka Y, Strick PL, 2013 Extended practice of a motor skill is associated with reduced metabolic activity in M1. Nat. Neurosci. 16, 1340–1347. [PubMed: 23912947]

Pons TP, Garraghty PE, Cusick CG, Kaas JH, 1985 The somatotopic organization of area 2 in macaque monkeys. J. Comput. Neurol. 241, 445–466.

Riehle A, Wirtssohn S, Grün S, Brochier T, 2013 Mapping the spatio-temporal structure of motor cortical LFP and spiking activities during reach-to-grasp movements. Front. Neural Circuits 7, 48. [PubMed: 23543888]

Rouse AG, Schieber MH, 2016 Spatiotemporal distribution of location and object effects in primary motor cortex neurons during reach-to-grasp. J. Neurosci. 36, 10640–10653. [PubMed: 27733614]

Ruiz O, Lustig BR, Nassi JJ, Cetin A, Reynolds JH, Albright TD, Callaway EM, Stoner GR, Roe AW, 2013 Optogenetics through windows on the brain in the non-human primate. J. Neurophysiol. 110, 1455–1467. [PubMed: 23761700]

Saleh M, Takahashi K, Hatsopoulos NG, 2012 Encoding of coordinated reach and grasp trajectories in primary motor cortex. J. Neurosci. 32, 1220–1232. [PubMed: 22279207]

Schieber MH, Hibbard LS, 1993 How somatotopic is the motor cortex hand area? Science 261, 489–492. [PubMed: 8332915]

Seelke AMH, Padberg JJ, Disbrow E, Purnell SM, Recanzone G, Krubitzer L, 2012 Topographic maps within brodmann's area 5 of macaque monkeys. Cereb Cortex 22, 1834–1850. [PubMed: 21955920]

Sessle BJ, Wiesendanger M, 1982 Structural and functional definition of the motor cortex in the monkey (Macaca fascicularis). J. Physiol. 323, 245–265. [PubMed: 7097574]

Shoham D, Grinvald a, 2001 The cortical representation of the hand in macaque and human area S-I: high resolution optical imaging. J. Neurosci. 21, 6820–6835. [PubMed: 11517270]

Sirotin YB, Hillman EMC, Bordier C, Das A, 2009 Spatiotemporal precision and hemodynamic mechanism of optical point spreads in alert primates. Proc. Natl. Acad. Sci. U S A 106, 18390–18395. [PubMed: 19828443]

Stepniewska I, Gharbawie OA, Burish MJ, Kaas JH, 2014 Effects of muscimol inactivations of functional domains in motor, premotor, and posterior parietal cortex on complex movements evoked by electrical stimulation. J. Neurophysiol. 111, 1100–1119. [PubMed: 24353298]

Tanigawa H, Lu HD, Roe AW, 2010 Functional organization for color and orientation in macaque V4. Nat. Neurosci. 13, 1542–1548. [PubMed: 21076422]

Tootell RB, Hamilton SL, Silverman MS, Switkes E, 1988 Functional anatomy of macaque striate cortex. I. Ocular dominance, binocular interactions, and baseline conditions. J. Neurosci. 8, 1500–1530. [PubMed: 3367209]

Umilta MA, Brochier T, Spinks RL, Lemon RN, 2007 Simultaneous recording of macaque premotor and primary motor cortex neuronal populations reveals different functional contributions to visuomotor grasp. J. Neurophysiol. 98, 488–501. [PubMed: 17329624]

Wang X, Liu Y, Li X, Zhang Z, Yang H, Zhang Y, Williams PR, Alwahab NSA, Kapur K, Yu B, Zhang Y, Chen M, Ding H, Gerfen CR, Wang KH, He Z, 2017 Deconstruction of corticospinal circuits for goal-directed motor skills. Cell 171, 440–455 e14. [PubMed: 28942925]

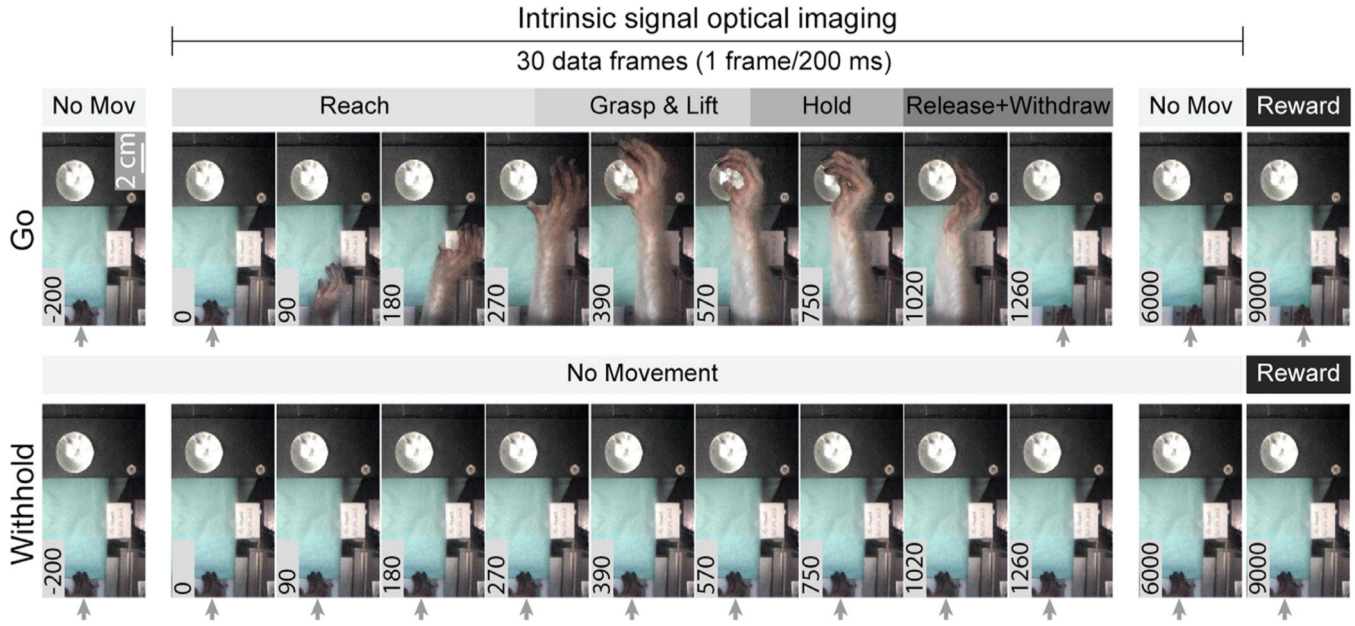

Fig. 1. Task phases in relation to intrinsic signal optical imaging.

(Top row) Still frames captured from a video recording of a representative trial in the Large Sphere/Go condition. Camera is directly overhead and task is performed here with the right forelimb. Time (ms) relative to reach onset is indicated in bottom left corner of each still frame. Approximate task phase and imaging time window are indicated above the still frames. (Bottom row) Frames from a representative trial in the Withhold condition. Both hands had to remain in the start position for the duration of the trial. Grey arrows point to the hand in the start position. LEDs (not shown) above the target object instructed the animal about condition type and task phase.

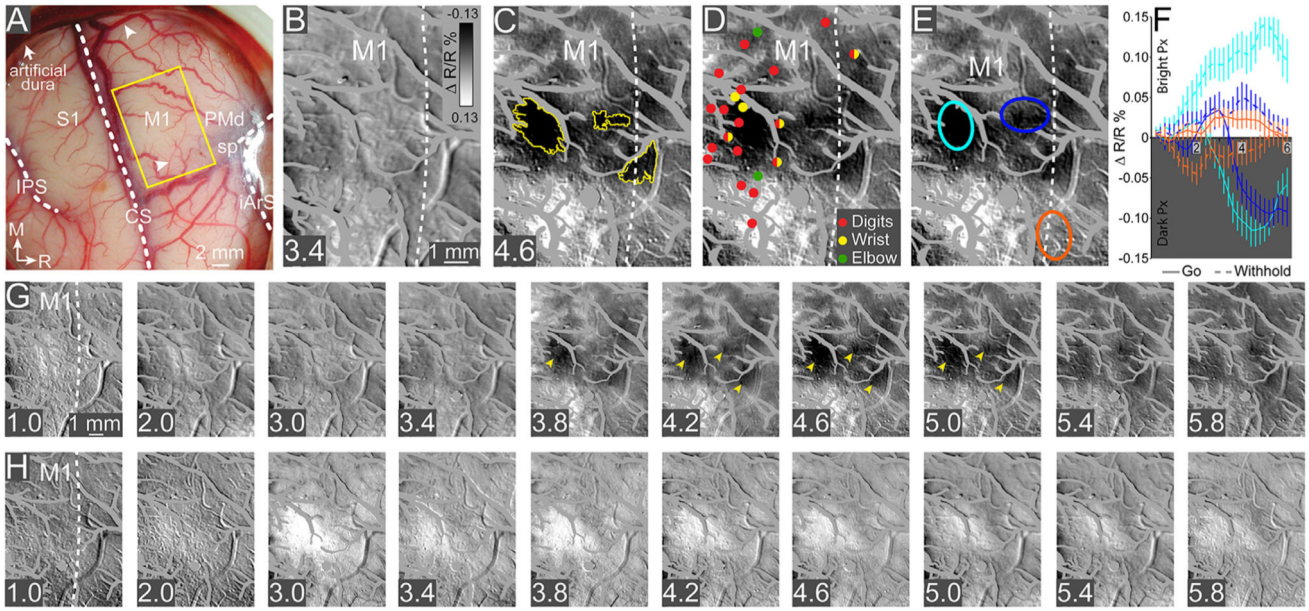

Fig. 2. M1 hand domain activation in the reach-to-grasp task.

Results from left hemisphere; task performed with right forelimb. Panels are reflected vertically to match the orientation of the right hemisphere. (A) Cropped image of optical imaging chamber. Native dura was surgically replaced with transparent membrane. White arrows point to blood vessels that are referenced in Fig. 5A. Yellow rectangle outlines cropping within the imaging field-of-view, which was centered onto primary motor cortex (M1). All subsequent panels match the location of the yellow rectangle. Major landmarks are depicted with dashed lines: central sulcus (CS), intraparietal sulcus (IPS), spur of arcuate sulcus (sp), and inferior arcuate sulcus (iArS). (B) Average (49 trials) optical image captured 3.4 s after reach onset in the Large Sphere/Go condition. No evidence of negative reflectance (pixel darkening). Scale and intensity bars apply to (B–E). (C) Three domains (yellow outline) approached peak size and darkness intensity ~4.6 s from reach onset. (D) Intracortical microstimulation sites superimposed onto duplicate of (C). Sites are color coded according to movement evoked. (E) Duplicate of (C) with 3 regions-of-interest (ROI, ~1.94 mm^2/ellipse) for time course analysis. (F) Time courses of average reflectance change (mean ± SEM) during Go (solid lines) and Withhold (dashed lines) conditions as measured from the 3 ROIs. Line plot colors match pertinent ROI colors. Negative values indicate pixel darkening (Dark Px). (G-H) Representative time series of optical images from (G) Large Sphere/Go condition, and (H) Withhold condition. Time (s) in relation to reach onset or withhold cue is indicated in bottom left hand corner of each frame. Intensity scale same as (B). (G) Spatiotemporal development of negative reflectance in M1. Yellow arrowheads point to the same domains in (C). (H) Positive reflectance (pixel brightening) is evident in the center of the FOV in most images. (B–H) Images were convolved with a 6.90 × 6.90 mm median filter and a 0.08 × 0.08 mm Gaussian filter to reduce low and high spatial frequency noise, respectively. Vascular noise masked with grey. Small gray circle masks artifact from an air bubble.

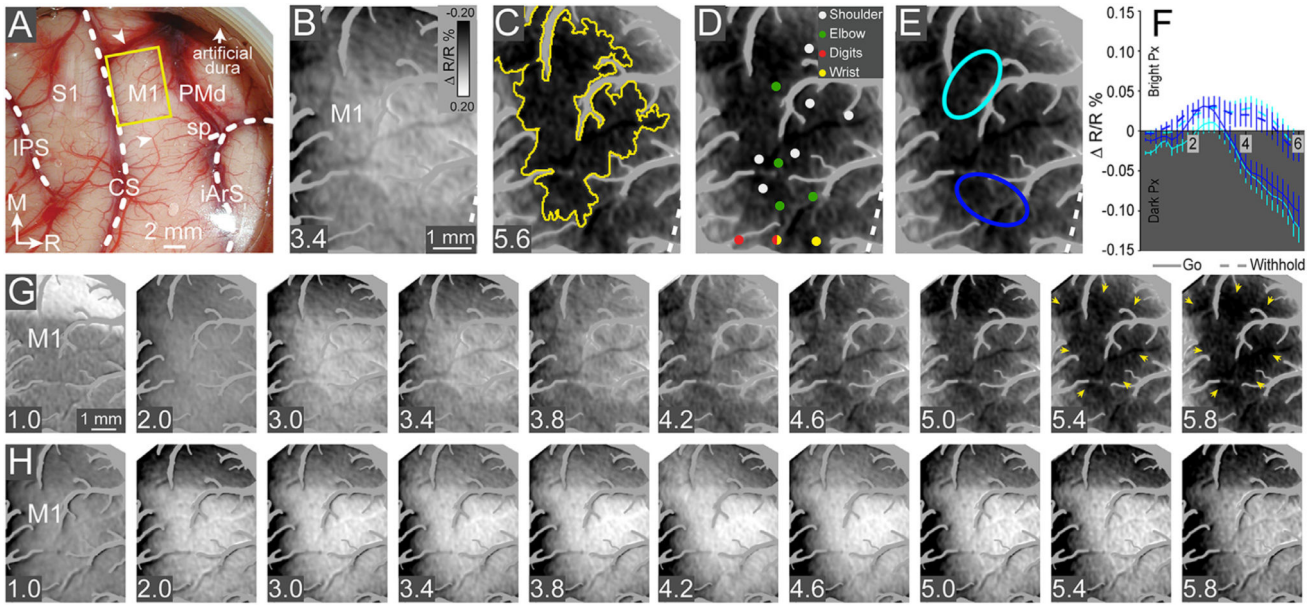

Fig. 3. M1 arm domain activation in the reach-to-grasp task.

Results from right hemisphere; task performed with left forelimb. Conventions follow Fig. 2. (A) Imaging field of view (yellow rectangle) was medial relative to the field-of-view in the opposite hemisphere. White arrows point to blood vessels that are referenced in Fig. 6A. (B) Average (73 trials) imaging frame captured 3.4 s after reach onset shows no pixel darkening. (C) The M1 domain (yellow outline) peaked in size and intensity ~5.6 s from reach onset. (D) The domain primarily overlapped ICMS sites that evoked shoulder and elbow movements. (E) Regions-of-interest (ROIs, ~1.98 mm ^{2} /ellipse) were placed in medial (cyan) and lateral (blue) aspects of the domain. (F) Time courses of average reflectance change (mean ± SEM) during Go (solid lines) and Withhold conditions (dashed lines) as measured from ROIs in (E). (G) Representative time series of optical images from (G) Large Sphere/Go condition, and (H) Withhold condition. (G) Yellow arrowheads approximately outline the activation domain. At 1.0 s, illumination shadow (horizontal line) is evident in top third of the optical image. (H) Pixel brightening is evident in the center of the FOV in most images. Illumination shadow is evident in the top third of optical images from 2.0 to 5.8 s. (B–H) Images were convolved with a 9.72 × 9.72 mm and 0.14 × 0.14 mm Gaussian filter to reduce low and high spatial frequency noise, respectively. Vascular noise masked in grey.

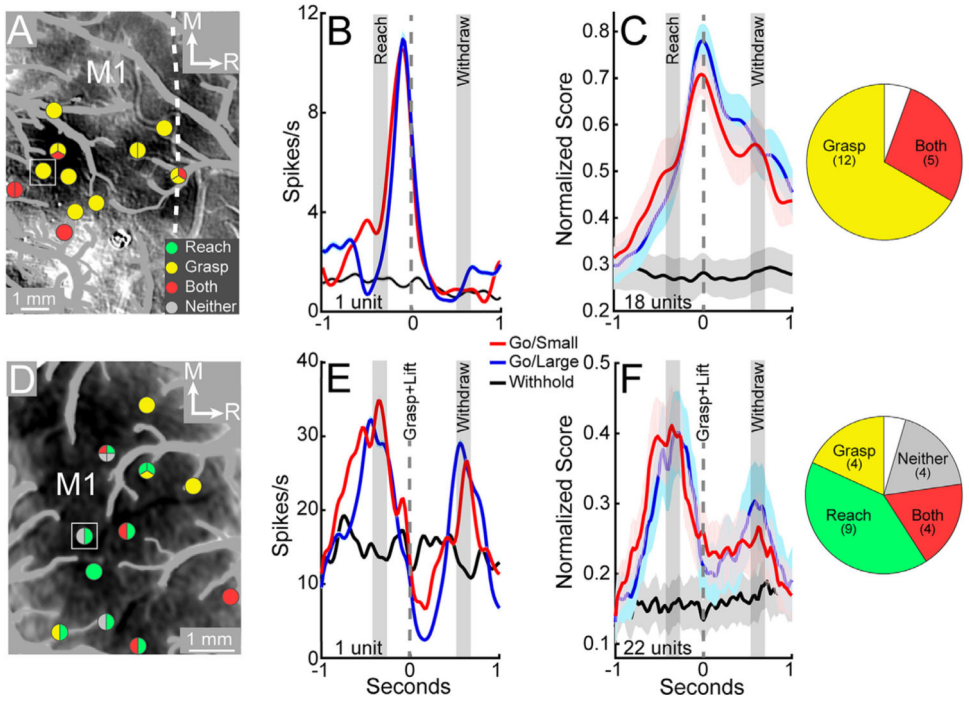

Fig. 4. Single unit recordings from M1 domains.

(A–C) Single unit recording results from the M1 hand domains. (A) Single unit recording sites (circles) superimposed on duplicate of Fig. 2C. Each circle is partitioned according to the number of units recorded at each site. Only task-related units (17/18 units) are shown. Each partition (single unit) is color coded according to task phase with highest firing rate (Bonferroni, $p<0.008$). (B) PSTH (mean ± SEM) from an example *Grasp unit*; recording location depicted with white square in (A). Time zero in the Go conditions is the point at which the hand grasped the object and started to lift it. Cue onset is time zero in the Withhold condition. Gray rectangles depict range of times for reach onset and withdrawal on set. Activity peaked during grasp completion. (C) Population response (mean ± SEM) for the 18 single units recorded from the M1 hand domain. Firing rates are normalized for all trials recorded from a given unit (highest firing rate = 1; lowest firing rate = 0). The population response peaked during grasp completion and the start of object lift. Pie chart shows the classification of the 18 units recorded in this domain. Number of units is in parentheses. Blank slice represents 1 unit that was not task-related. Note, the absence of *Reach units and Neither units* in this domain. (D-F) Single unit recording results from the M1 arm domain; conventions follow (A–C). (D) Locations of task-related units (21/22 units) superimposed on duplicate of Fig. 3C. (E) PSTH (mean ± SEM) from a representative *Reach unit;* recording location depicted with white square in (D). Activity peaked during reach onset and again during forelimb withdrawal. (F) Population response (mean ± SEM) for the 22 single units recorded from the M1 arm domain. The population response peaked during reach onset with a second smaller peak during forelimb withdrawal. Pie chart shows the classification of the 22 units recorded in this domain. Blank slice represents 1 unit that was not task-related.

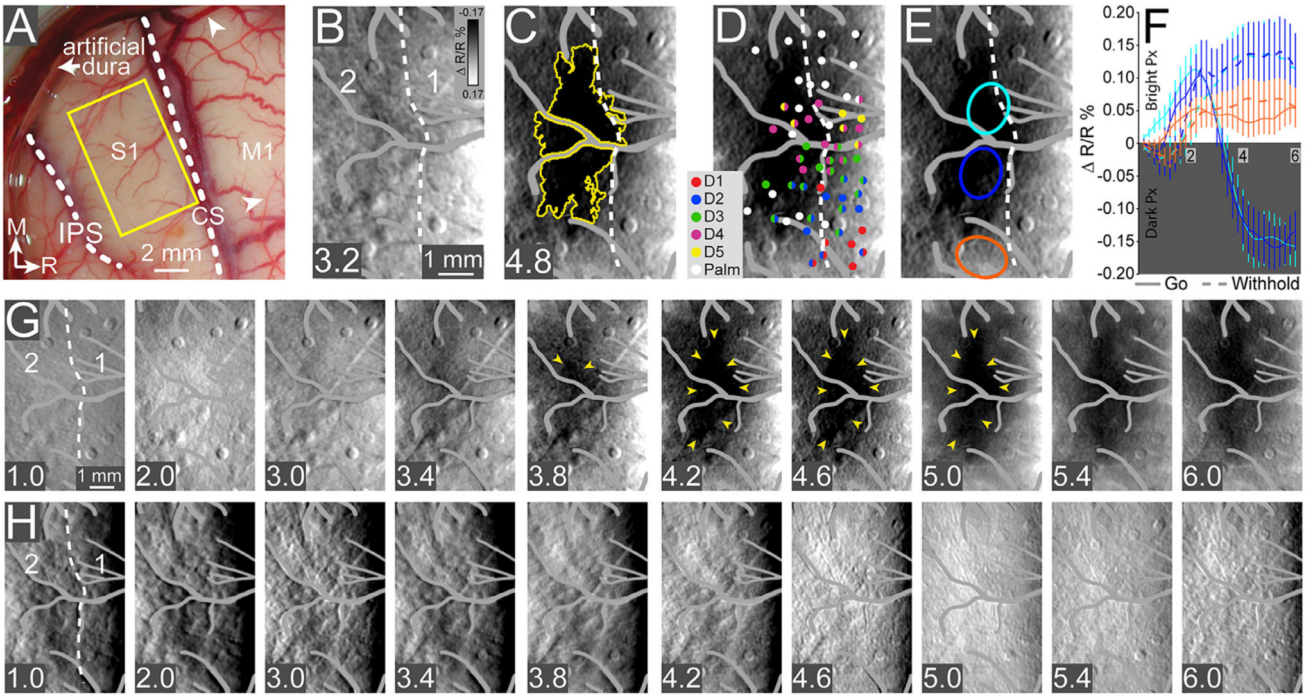

Fig. 5. S1 domain activation in the reach-to-grasp task.

Results from left hemisphere; task performed with right forelimb. Panels are vertically reflected to match the orientation of the right hemisphere. Layout and conventions are similar to Fig. 2. (A) Imaging field-of-view (yellow rectangle) was centered on somatosensory areas 1 and 2. White arrowheads reference blood vessel landmarks in Fig. 2A. (B) Average (33 trials) optical image shows no pixel darkening during the initial 3.2 s from reach onset. (C) Yellow arrowheads approximately outline the S1 domain as it approached peak size and intensity, 4.8 s from reach onset. (D) Multi-unit recording sites are superimposed onto duplicate of (C). Sites are color coded according to receptive fields. The S1 domain overlapped primarily with the representations of digits 2, 3, 4, and parts of the palm. (E) Regions-of-interest (ROIs, ~1.37 mm^2 /ellipse) for measuring time courses during Go and Withhold conditions. (F) Timecourses of average reflectance change (mean ± SEM) measured during Go (solid line) and Withhold (dashed line) conditions. Line plots match ROI colors in (E). (G) Representative optical images show the spatiotemporal development of the S1 domain (approximately outlined with yellow arrowheads) in the Go condition. (H) Representative optical images show the gradual pixel brightening in the Withhold condition. (B–H) Images were convolved with a 11.80 × 11.80 mm median filter and a 0.11 × 0.11 mm Gaussian filter to reduce low and high spatial frequency noise, respectively. Vascular noise masked with grey.

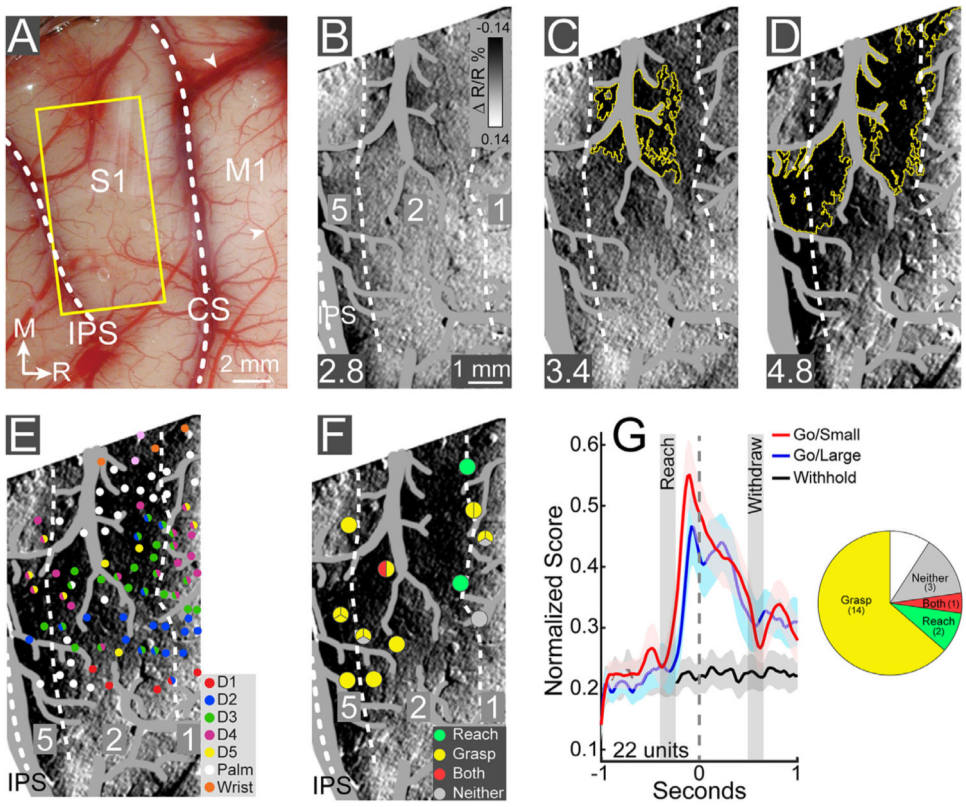

Fig. 6. Single unit recordings from the S1 domain.

Results from the right hemisphere; task was performed with the left forelimb. (A) Yellow rectangle outlines cropping within the imaging field-of-view. White arrowheads reference blood vessel landmarks in Fig. 3A. (B) Average (65 trials) optical image shows no pixel darkening during the initial 2.8 s from reach onset. Scale and intensity bars apply to (B–D). (C) Pixels start to darken (yellow outline) by 3.4 s from reach onset. (D) S1 domain near its peak size and intensity at 4.8 s from reach onset. (B–F) Images were convolved with a 11.11 × 11.11 mm median filter and a 0.08 × 0.08 mm Gaussian filter to reduce low and high spatial frequency noise, respectively. Vascular noise masked with grey. (E) Multi-unit recording sites are superimposed onto a duplicate of (D). The S1 domain overlapped primarily with somatosensory representations of digits 2, 3, 4, and parts of the palm. (F) Single unit recording sites (i.e., circles) partitioned according to number of units recorded. Only task-related units (20/22 units) are shown. (G) Population response (mean ± SEM) for the 22 units recorded from the S1 domain. Time zero (dashed line) marks the conclusion of object grasp and start of object lift (same as Fig. 4). Pie chart shows that most single units in this domain were *Grasp units*. Blank slice represents two units that were not task-related.

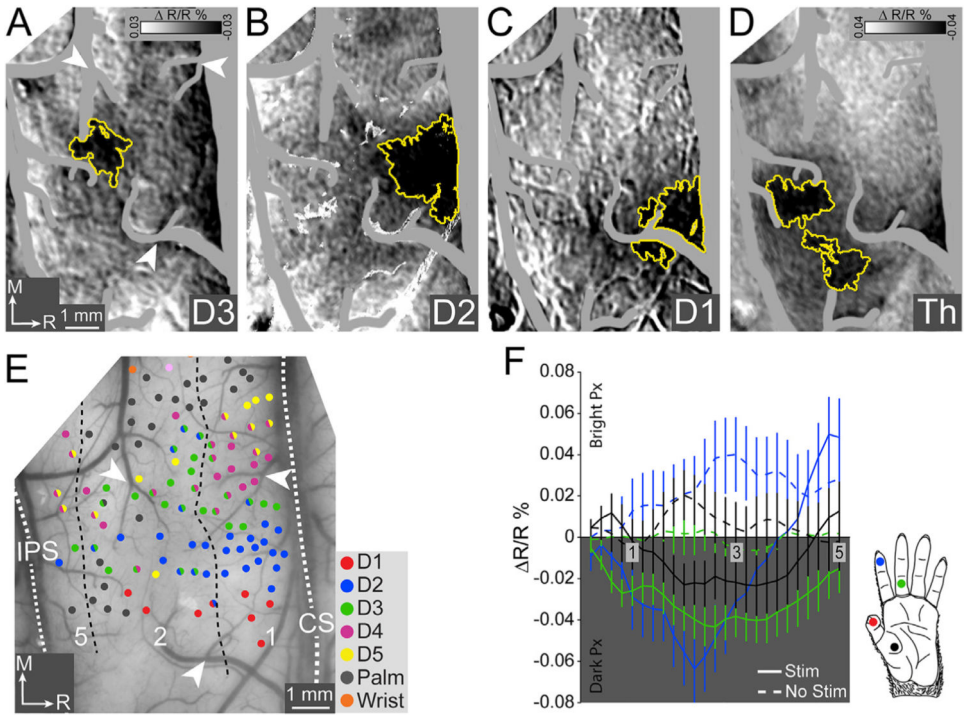

Fig. 7. Vibrotactile stimulation activates focal domains in S1.

Results from right hemisphere; stimulation delivered to left hand. (A–D) Average (69–70 trials) optical imaging maps in response to vibrotactile stimulation (2 mm probe diameter) tested on 4 locations on the glabrous side of the hand. Activation domain is outlined (yellow) in each panel. Each optical image is the subtraction of 2 conditions in 3 data frames captured 1.4–2.4 s from stimulation onset. (A) D3 (proximal D3 minus Blank). (B) D2 (distal D2 minus distal D3). (C) D1 (distal D1 minus proximal D2). (D) Thenar (distal thenar minus Blank). (A-D) Images were convolved with a 9.72 × 9.72 mm median filter and a 0.14 × 0.14 mm Gaussian filter to reduce low and high spatial frequency noise, respectively. Vascular noise masked with grey. White arrowheads in (A) and (E) reference the same blood vessel landmarks. (E) Microelectrode recording sites (circles) classified according to receptive fields. (F) Time course of reflectance change (mean ± SEM) in response to vibrotactile stimulation of D3 (green), D2 (blue), and thenar (black). One ROI (~0.26 mm^2 circle) was centered on each domain. Time courses were measured during tactile stimulation (solid line) and no stimulation (dashed line). Line plots are colored according to pertinent stimulation location shown on hand drawing. Time course for D1 stimulation overlapped with the Thenar time course and was therefore not shown.